Computation of Transfer Maps from Surface Data with Applications to ILC Damping Ring Wigglers

Chad Mitchell and Alex Dragt
University of Maryland

March 2007 Version

Abstract

Simulations indicate that the dynamic aperture of proposed ILC Damping Rings is dictated primarily by the nonlinear properties of their wiggler transfer maps. Wiggler transfer maps in turn depend sensitively on fringe-field and high-multipole effects. Therefore it is important to have detailed magnetic field data including knowledge of high spatial derivatives. This talk describes how such information can be extracted reliably from 3-dimensional field data on a grid as provided, for example, by various 3-dimensional field codes available from Vector Fields. The key ingredient is the use of surface data and the smoothing property of the inverse Laplacian operator.

Surface Methods in ILC DR Lattice Design

- Developing methods to produce accurate transfer maps for realistic beam-line elements.

- Such methods use accurate 3-d field data provided by finite element modeling (Opera) to incorporate fringe field effects, nonlinear multipoles.

- Once accurate transfer maps have been found for individual beam-line elements, one can determine all single-particle properties of the ring: dynamic aperture, tunes, chromaticities, anharmonicities, linear and nonlinear lattice functions, etc.

- Key is the use of surface data to compute interior data. Surface must enclose design trajectory and lie within all iron or other sources.

Objective

- To obtain an accurate representation of the interior field that is analytic and satisfies Maxwell equations exactly. We want a vector potential that is analytic and $\nabla \times \nabla \times \boldsymbol{A} = 0$.

- Use B-V data to find an accurate series representation of interior vector potential through order N in (x,y) deviation from design orbit.

$$A_x(x,y,z) = \sum_{l=1}^{L} a_l^x(z) P_l(x,y)$$

L=27 for N=6

- Use a Hamiltonian expressed as a series of homogeneous polynomials

$$K = -\sqrt{\frac{(p_t + q\phi)^2}{c^2} - (\boldsymbol{p}_\perp - q\boldsymbol{A}_\perp)^2} - qA_z = \sum_{s=1}^{S} h_s(z) K_s(x, p_x y, p_y, \tau, p_\tau)$$

S=923 for N=6

- We compute the design orbit and the transfer map about the design orbit to some order. We obtain a factorized symplectic map for single-particle orbits through the beamline element:

$$M = R_2 e^{:f_3:} e^{:f_4:} e^{:f_5:} e^{:f_6:} \ldots$$

Advantages of Surface Fitting

- Maxwell equations are exactly satisfied.
- Error is globally controlled. The error must take its extrema on the boundary, where we have done a controlled fit.
- Careful benchmarking against analytic results for arrays of magnetic monopoles.
- Insensitivity to errors due to inverse Laplace kernel smoothing. Improves accuracy in higher derivatives. Insensitivity to noise improves with increased distance from the surface: advantage over circular cylinder fitting.

Realistic transfer maps can now be computed for all beamline elements of the damping ring using surface methods:

- Solenoids and multipoles -- circular cylinder (M. Venturini)
- RF cavities -- circular cylinder (D. Abell)
- Wiggler magnets -- elliptical / circular cylinder (C. Mitchell, M. Venturini)
- Bending dipoles -- bent box / bent cylinder (C. Mitchell, P. Walstrom)

Fitting Wiggler Data Using Elliptical Cylinder

- Data on regular Cartesian grid

4.8cm in x, dx=0.4cm

2.6cm in y, dy=0.2cm

480cm in z, dz=0.2cm

- Field components Bx, By, Bz in one quadrant given to a precision of 0.05G.

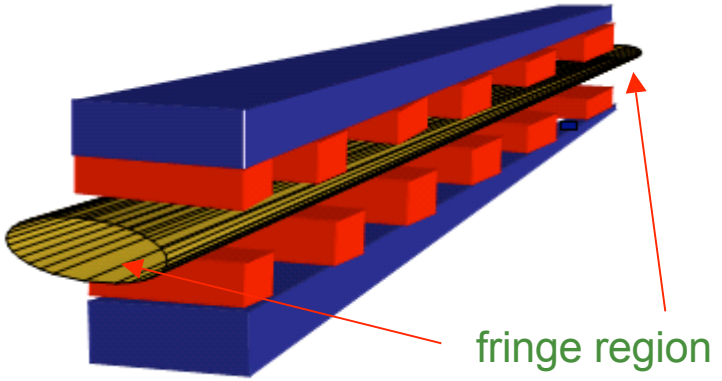

- Place an imaginary elliptic cylinder between pole faces, extending beyond the ends of the magnet far enough that the field at the ends is effectively zero.

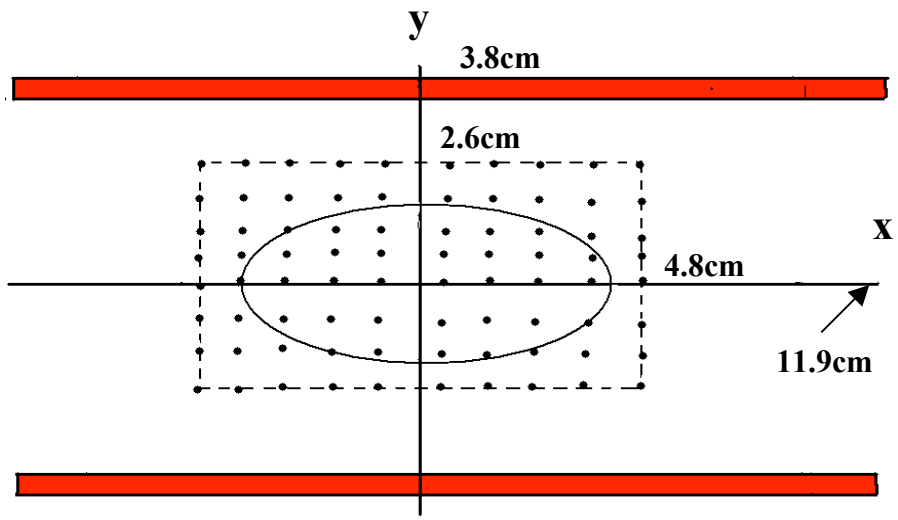

- Fit data onto elliptic cylindrical surface using bicubic interpolation to obtain the normal component on the surface.

- Compute the interior vector potential and all its desired derivatives from surface data.

Fit to the Proposed ILC Wiggler Field Using Elliptical Cylinder

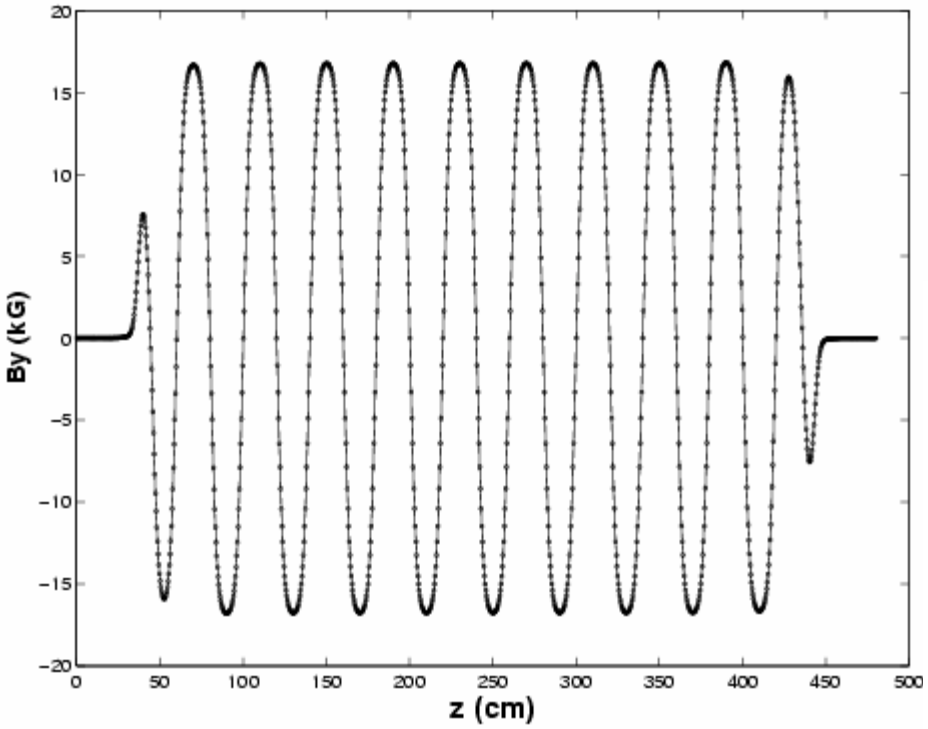

Fit to vertical field By
at x=0.4cm, y=0.2cm.

Note precision of data.

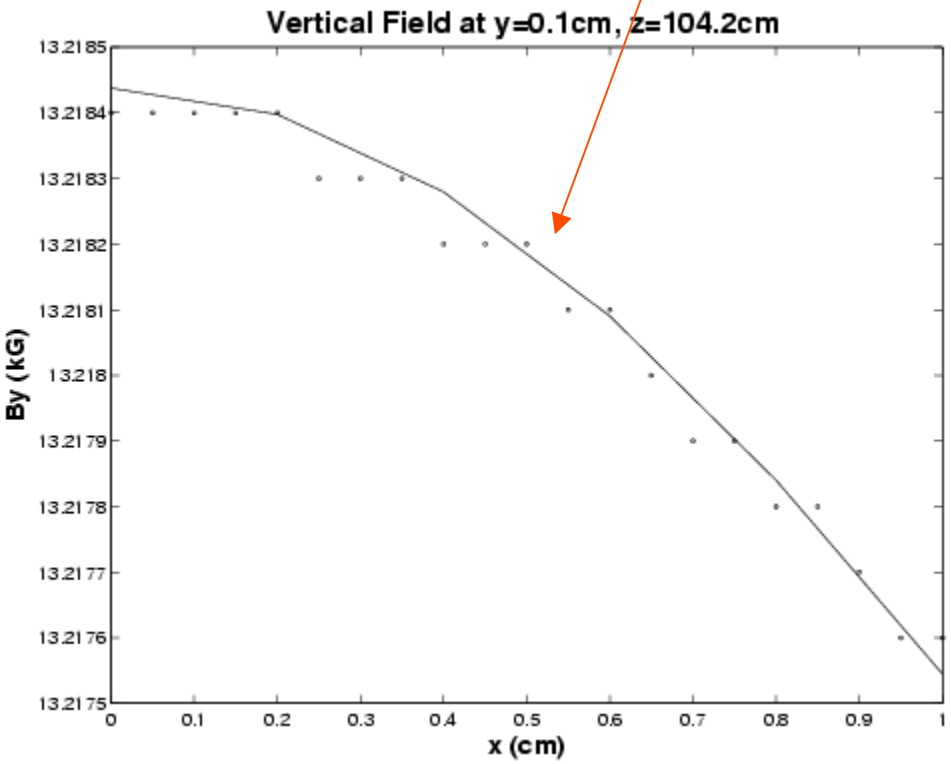

Residuals ~ 0.5G / 17kG

Fit to the Proposed ILC Wiggler Field Using Elliptical Cylinder

No information about Bz was used to create this plot.

Fit to longitudinal field Bz at x=0.4cm, y=0.2cm.

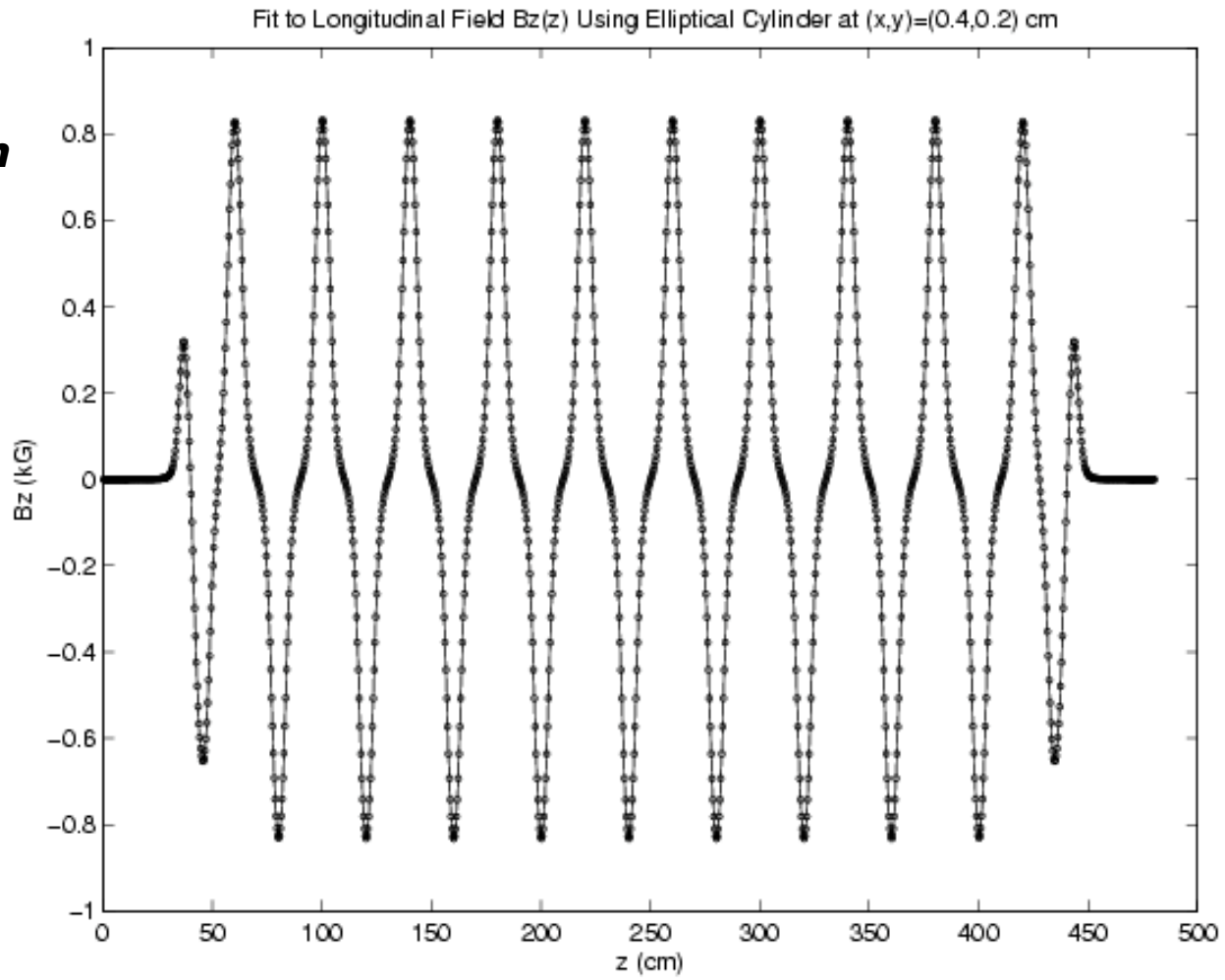

Dipole Field Test for Elliptical Cylinder

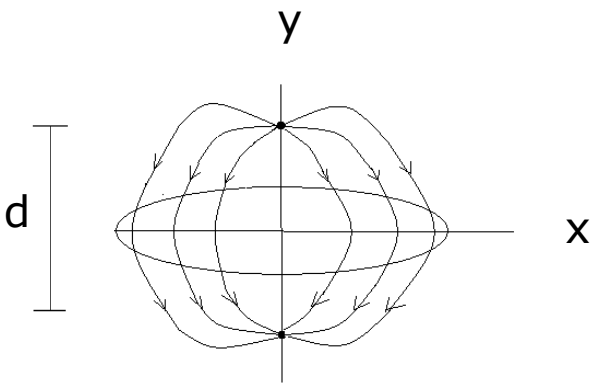

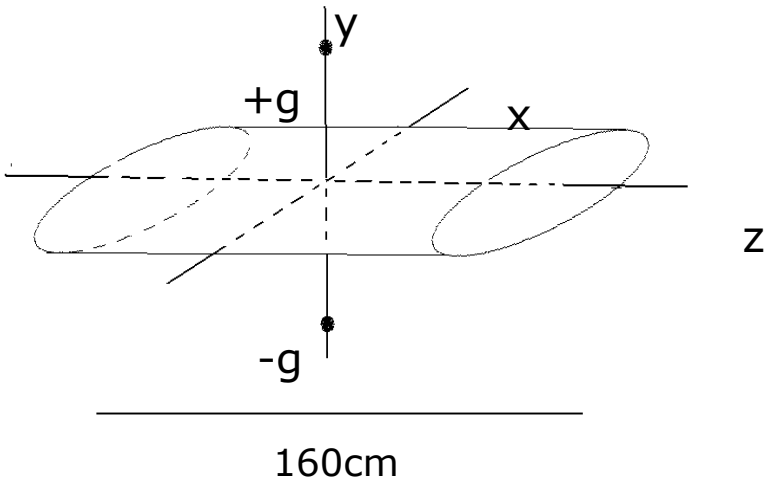

- Simple field configuration in which all derivatives of the field and on-axis gradients can be determined analytically.
- Tested for two different aspect ratios: 4:3 and 5:1.
- Direct solution for interior scalar potential accurate to 3×10^{-10}: set by convergence and roundoff.
- Computation of on-axis gradients C1, C3, C5 accurate to 2×10^{-10} before final Fourier transform accurate to 2.6×10^{-9} after final Fourier transform.

Pole location: d=4.7008cm

Pole strength: $g=0.3Tcm^2$

Semimajor axis: 1.543cm/4.0cm

Semiminor axis: 1.175cm/0.8cm

Boundary to pole: 3.526cm/3.9cm

Focal length: f=1.0cm/3.919cm

Bounding ellipse: u=1.0/0.2027

Remarks about Geometry

- For the circular and elliptical cylinder, only the normal component of on the surface was used to determine interior fields.

- The circular and elliptical cylinder are special in that Laplace's equation is separable for these domains.

- Laplace's equation is not separable for more general domains, e.g. a bent box.

- Surface data for general domains can again be used to fit interior data provided *both* $\boldsymbol{B}_{normal}$ and ψ are available on the surface. Analogous smoothing behavior is again expected to occur.

Table F.1: Separable Coordinates for the Helmholtz Equation

Commuting operators S_1, S_2	Separable coordinates	Solutions
1. P_2^2, P_3^2	Cartesian x, y, z	Exponentials
2. J_3^2, P_3^2	Cylindrical $x = r\cos\phi$ $y = r\sin\phi$, $z = z$	Bessel functions
3. $\{J_3, P_2\}$, P_3^2	Parabolic cylindrical $x = (\xi^2 - \eta^2)/2$ $y = \xi\eta$, $z = z$	Parabolic cylinder functions
4. $J_3^2 + d^2P_1^2$, P_3^2	Elliptic cylindrical $x = d\cosh u\cos v$ $y = d\sinh u\sin v$, $z = z$	Mathieu functions
5. $\mathbf{J}\cdot\mathbf{J}$, J_3^2	Spherical $x = \rho\sin\theta\cos\phi$ $y = \rho\sin\theta\sin\phi$, $z = \rho\cos\theta$	Spherical harmonics
6. $\mathbf{J}\cdot\mathbf{J} - a^2(P_1^2 + P_2^2)$, J_3^2	Prolate spheroidal $x = a\sinh\eta\sin\alpha\cos\phi$ $y = a\sinh\eta\sin\alpha\sin\phi$ $z = a\cosh\eta\cos\alpha$	Spheroidal wave functions Ps_n^m
7. $\mathbf{J}\cdot\mathbf{J} + a^2(P_1^2 + P_2^2)$, J_3^2	Oblate spheroidal $x = a\cosh\eta\sin\alpha\cos\phi$ $y = a\cosh\eta\sin\alpha\sin\phi$ $z = a\sinh\eta\cos\alpha$	Spheroidal wave functions
8. $\{J_1, P_2\} - \{J_2, P_1\}$, J_3^2	Parabolic $x = \xi\eta\cos\phi$ $y = \xi\eta\sin\phi$, $z = (\xi^2 - \eta^2)/2$	Confluent hypergeomentric functions
9. $J_3^2 - c^2P_3^2 +$ $c(\{J_2, P_1\} + \{J_1, P_2\})$, $c(P_2^2 - P_1^2) +$ $\{J_2, P_1\} - \{J_1, P_2\}$	Paraboloidal $x = 2c\cosh\alpha\cos\beta\sinh\gamma$ $y = 2c\sinh\alpha\sin\beta\cosh\gamma$ $z = c(\cosh 2\alpha + \cos 2\beta - \cosh 2\gamma)/2$	
10. $P_1^2 + aP_2^2 +$ $(a+1)P_3^2 + \mathbf{J}\cdot\mathbf{J}$, $J_2^2 + a(J_1^2 + P_3^2)$	Ellipsoidal $x = \left(\frac{(\mu-a)(\nu-a)(\rho-a)}{a(a-1)}\right)^{1/2}$, $y = \left(\frac{(\mu-1)(\nu-1)(\rho-1)}{1-a}\right)^{1/2}$, $z = (\mu\nu\rho/a)^{1/2}$	Ellipsoidal wave functions el_n^m
11. $\mathbf{J}\cdot\mathbf{J}$, $J_1^2 + bJ_2^2$	Conical $x = r\left(\frac{(b\mu-1)(b\nu-1)}{1-b}\right)^{1/2}$, $y = r\left(\frac{b(\mu-1)(\nu-1)}{b-1}\right)^{1/2}$, $z = r(b\mu\nu)^{1/2}$	Lamé polynomials

131

P_3^2

Laplace equation separates fully in 11 orthogonal coordinate systems.

straight-axis geometries

Separated solutions are simultaneous eigenstates of two second-order symmetry operators:

$$\nabla^2\Psi_{kl} = 0 \qquad S_1\Psi_{kl} = k^2\Psi_{kl} \qquad S_2\Psi_{kl} = l^2\Psi_{kl}$$

Pro: Solutions have known, optimal convergence properties.

Con: Difficult functions, techniques strongly dependent on particular surface geometry.

The Bent Box and Other Geometries

The previous techniques can be used effectively for straight-axis magnetic elements.

For elements with significant sagitta, such as dipoles with large bending angles, we must generalize to more complicated domains in which Laplace's equation is not separable.

Given both ψ and $\boldsymbol{B}_{normal}$ on a surface enclosing the beam, the magnetic vector potential in the interior can be determined by the integration of surface data against a geometry-independent kernel.

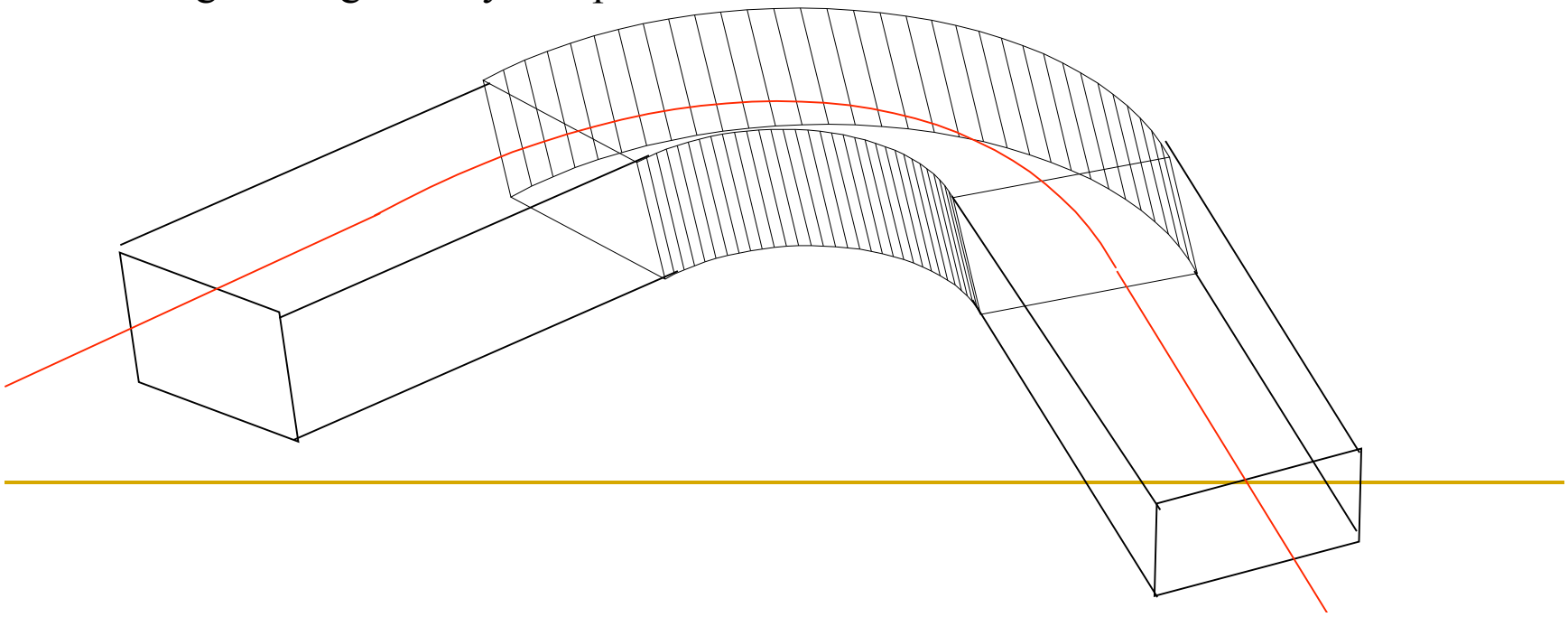

Application of Helmholtz Theorem

Decompose the interior field into a divergence and curl

$$F = \nabla \times A + \nabla \Phi$$

of the form:

$$\mathbf{A}(r) = -\frac{1}{4\pi}\int_S \frac{n(r') \times F(r')}{|r - r'|} dS' + \frac{1}{4\pi}\int_V \frac{\nabla' \times F(r')}{|r - r'|} dV'$$

$$\Phi(r) = -\frac{1}{4\pi}\int_S \frac{n(r') \cdot F(r')}{|r - r'|} dS' - \frac{1}{4\pi}\int_V \frac{\nabla' \cdot F(r')}{|r - r'|} dV'$$

In the absence of sources, we may write potentials in terms of surface data:

$$A^t(r) = -\frac{1}{4\pi}\int_S \frac{n(r') \times B(r')}{|r - r'|} dS' \quad \longleftarrow \quad \text{tangential components}$$

$$\Phi^n(r) = \frac{1}{4\pi}\int_S \frac{n(r') \cdot B(r')}{|r - r'|} dS' \quad \longleftarrow \quad \text{normal component}$$

To compute a Lie map from the Hamiltonian we require $\mathbf{B} = \nabla \times \mathbf{A}$ alone.

$$\nabla \times A^n = \nabla \Phi^n \quad ?$$

Dirac monopole construction

We exploit the vector potential of a Dirac monopole of charge g:

$$\boldsymbol{A}_m(r) = -\frac{g}{4\pi}\int_L d\boldsymbol{r}' \times \nabla\left(\frac{1}{|\boldsymbol{r}-\boldsymbol{r}'|}\right)$$

where L is a curve extending from the monopole source to infinity. We choose L to be a ray in the direction defined by $\boldsymbol{m}$. Then

$$\boldsymbol{A}_m(\boldsymbol{r}) = \frac{g\boldsymbol{m}\times(\boldsymbol{r}-\boldsymbol{r}')}{4\pi\,|\boldsymbol{r}-\boldsymbol{r}'|(|\boldsymbol{r}-\boldsymbol{r}'|-\boldsymbol{m}\cdot(\boldsymbol{r}-\boldsymbol{r}'))}$$

This vector potential has the desired property that

$$F_m(r) = \nabla \times A_m(r) = -\frac{g}{4\pi}\nabla\left(\frac{1}{|r-r'|}\right)$$

at all points away from the ray L. Furthermore, $\nabla \cdot A_m = 0$.

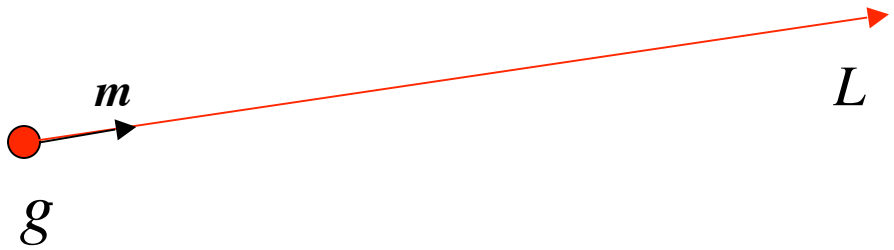

We define a vector field

$$\boldsymbol{A}^n(\boldsymbol{r}) = \int_S [\boldsymbol{n}(\boldsymbol{r}') \cdot \boldsymbol{B}(\boldsymbol{r}')]\boldsymbol{G}^n(\boldsymbol{r};\boldsymbol{r}',\boldsymbol{m}(\boldsymbol{r}'))dS'$$

where the kernel is given by the vector potential of a monopole at a point $\boldsymbol{r}'$:

$$\boldsymbol{G}^n(\boldsymbol{r};\boldsymbol{r}',\boldsymbol{m}) = \frac{\boldsymbol{m} \times (\boldsymbol{r} - \boldsymbol{r}')}{4\pi\,|\boldsymbol{r} - \boldsymbol{r}'|\left[|\boldsymbol{r} - \boldsymbol{r}'| - \boldsymbol{m} \cdot (\boldsymbol{r} - \boldsymbol{r}')\right]}$$

Here $\boldsymbol{m}$ is allowed to vary over the surface. This vector potential will satisfy

$$\nabla \times A^n(r) = \int_S [n(r') \cdot B(r')]\nabla \times G^n(r;r',m(r'))dS'$$

$$= \int_S \frac{[n(r') \cdot B(r')]}{4\pi} \nabla\left(\frac{1}{|r - r'|}\right) dS' = \nabla\Phi^n$$

We also rewrite $\boldsymbol{A}^t$ in terms of a scalar potential on the surface $\boldsymbol{B} = \nabla\psi$:

$$\boldsymbol{A}^t(\boldsymbol{r}) = \frac{1}{4\pi}\int_S \psi(\boldsymbol{r}')\boldsymbol{G}^t(\boldsymbol{r};\boldsymbol{r}')dS'$$

$$\boldsymbol{A} = \boldsymbol{A}^n + \boldsymbol{A}^t$$

We have the kernels:

$$\boldsymbol{G}^n(\boldsymbol{r};\boldsymbol{r}',\boldsymbol{m}) = \frac{\boldsymbol{m}\times(\boldsymbol{r}-\boldsymbol{r}')}{4\pi\,|\boldsymbol{r}-\boldsymbol{r}'|\left[|\boldsymbol{r}-\boldsymbol{r}'|-\boldsymbol{m}\cdot(\boldsymbol{r}-\boldsymbol{r}')\right]}$$

normal component

$$\boldsymbol{G}^t(\boldsymbol{r};\boldsymbol{r}') = \frac{\boldsymbol{n}(\boldsymbol{r}')\times(\boldsymbol{r}-\boldsymbol{r}')}{|\boldsymbol{r}-\boldsymbol{r}'|^3}$$

tangential components

where $\boldsymbol{m}$ is a unit vector pointing along some line that does not intersect the interior (a Dirac string), and $\boldsymbol{n}$ is the unit normal to the surface at $\boldsymbol{r}'$.

The kernels $\boldsymbol{G}^n$ and $\boldsymbol{G}^t$ are analytic in the interior. Given a point along the design orbit, we may construct a power series for $\boldsymbol{A}$ about $\boldsymbol{r}_d$ by integrating against the power series for the $\boldsymbol{G}$'s . Writing $\delta\boldsymbol{r} = \delta x\hat{\boldsymbol{e}}_x + \delta y\hat{\boldsymbol{e}}_y$,

$$\boldsymbol{G}(\boldsymbol{r}_d+\delta\boldsymbol{r};\boldsymbol{r}',\boldsymbol{n}) = \sum_{\alpha=1}^{L}\boldsymbol{G}_\alpha(\boldsymbol{r}_d;\boldsymbol{r}',\boldsymbol{n})P_\alpha(\delta x,\delta y)$$

This has been implemented numerically.

Code accepts as input 3d data of the form $(\boldsymbol{B},\psi)$ on a mesh and will produce as output:

1) Vector potential A at any interior point (gauge specified by orientation of strings)
2) Taylor coefficients of A about any design point through degree N

which in turn are used to compute…

3) Interior field B at any point
4) Taylor coefficients of B about any point
5) $\nabla \cdot A, \quad \nabla \times A, \quad \nabla \cdot B, \quad \nabla \times B$
   as Taylor series through degree N-1

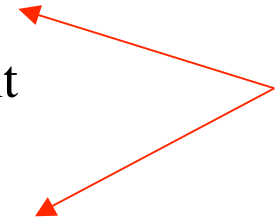

Code produces interior fits that satisfy Maxwell's equations exactly and even if the required surface integrals are performed approximately.

Transfer maps are then computed from the Taylor expansion of $\boldsymbol{A}$ along the design orbit.

Benchmarks for various domains

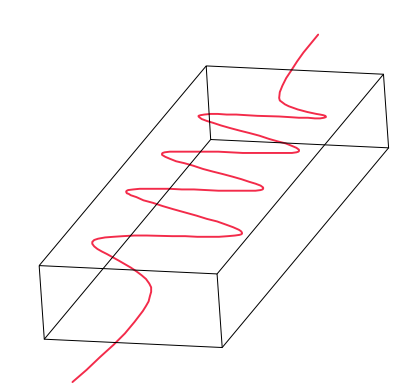

straight box

sphere

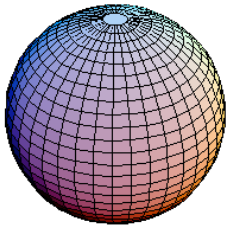

torus

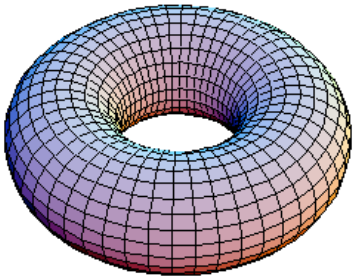

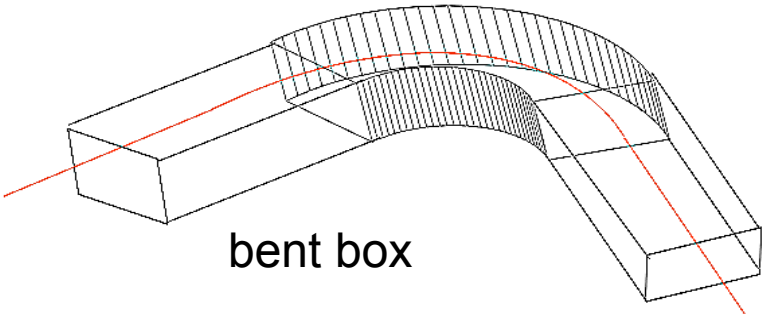

bent box

The procedure has been benchmarked for the above domains using arrays of magnetic monopoles to produce test fields. Power series for the components of $\boldsymbol{B}$ at a given point $\boldsymbol{r}_d$ are computed from the power series for $\boldsymbol{A}$. These results can be compared to the known Taylor coefficients of the field. We find, using a surface fit that is accurate to 10^{-4} , that all computed coefficients are accurate to 10^{-6}.

Similarly, we verify that $\nabla \cdot \boldsymbol{B} = 0$, $\nabla \times \boldsymbol{B} = 0$, and $\nabla \cdot \boldsymbol{A} = 0$ to machine precision.

Box Fit to ILC Wiggler Field

As an additional test, data provided by Cornell of the form (B_z, B_x, B_y, ψ) at grid points was fit onto the surface of a nearly-straight box filling the domain covered by the data. Box: 10 x 5 x 480cm Mesh: 0.2 x 0.4 x 0.2cm

Using this surface data, the power series for the vector potential was computed about several points in the interior. From this, the value of **B** was computed at various interior points and compared to the initial data.

interior points

Difference	(0.4, 0.2, 31.2) cm	(2, 2, 1) cm	(0, 1.4, 31.2) cm
Bx (G)	0.0417	0.187	0.230
By (G)	0.299	2.527	0.054
Bz (G)	0.161	0.626	0.916

Peak field=17kG Largest error/peak ~ 10^{-4}

Properties of solution:

- Guaranteed to satisfy Maxwell's equations exactly.
- Sources of error are controlled: surface interpolation and multivariable integration--can be treated as error in the surface functions $\boldsymbol{B}_{normal}$ and ψ .
- Error is globally bounded.
- High-frequency random numerical errors on the surface are damped in the interior (smoothing).

Challenges:

Reduce runtime. Operation count ~ LMNp. Computation can be parallelized.

L - number of points evaluated along design orbit
M - number points on surface mesh
N - degree of coefficients required by Lie map
p(N) - operations required by TPSA expansion of kernel

Smoothing of surface errors: an illustration

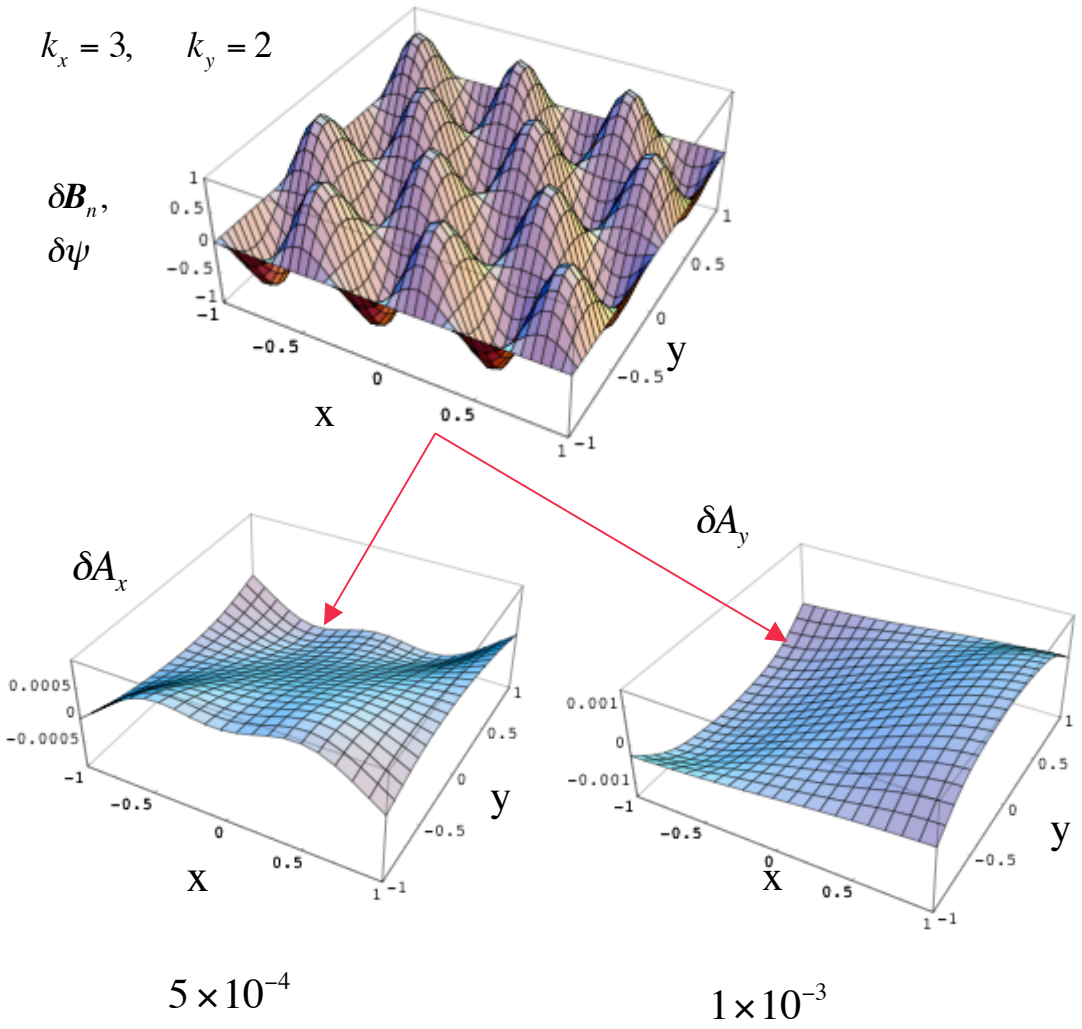

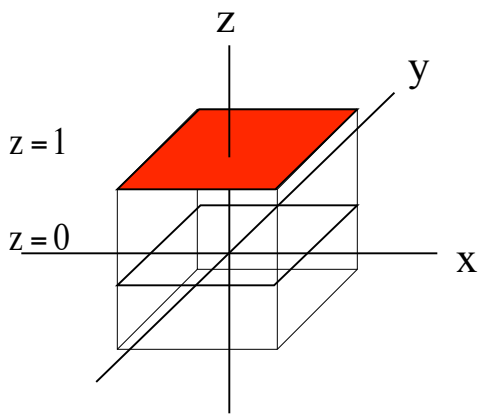

Surface harmonic $\mathbf{k}' = (k_x', k_y')$ added.

Kernels are analytic in (x, y, x', y'), so Fourier coefficients decay as

$$\left| g(\mathbf{k}, \mathbf{k}') \right| \le C \exp(-\lambda \cdot \mathbf{k}) \exp(-\lambda' \cdot \mathbf{k}')$$

Error in the plane is suppressed:

$$\delta A_\alpha = \pi^2 \sum_k g(\mathbf{k}, \mathbf{k}') \sin(k_x \pi x) \sin(k_y \pi y)$$

Contributions to ILC Damping Ring Studies

- Characterize all beamline elements by realistic symplectic transfer maps in Lie form $M = R_2 e^{:f_3:} e^{:f_4:} e^{:f_5:} e^{:f_6:} \ldots$

- Potential to compute all single-particle properties of the DR from a single combined one-turn map, using only real field data for the entire ring.

- Includes all fringe-field effects on dynamic aperture, tunes, chromaticities, anharmonicities, linear and nonlinear lattice functions, etc.

- Can be used to check models of beamline elements, but use of models is no longer required.

- Could produce hybrid code using both Lie maps and PIC-computed space charge effects.